Supporting Information

A Universal Model for Energy Level Alignment at Interfaces of Hole-Collecting Monolayers in p-i-n Perovskite Solar Cells

*Aruto Akatsuka, Minh Anh Truong, Atsushi Wakamiya, Gaurav Kapil, Shuzi Hayase, Hiroyuki Yoshida**

A. Akatsuka, H. Yoshida
Graduate School of Engineering, Chiba University, 1-33 Yayoi-Cho, Inage-ku, Chiba, 263-8522, Japan
E-mail: hyoshida@chiba-u.jp

M. A. Truong, A. Wakamiya
Institute for Chemical Research, Kyoto University, Gokasho, Uji, Kyoto, 611-0011, Japan

G. Kapil, S. Hayase
i-Powered Energy System Research Center (i-PERC), The University of Electro Communications, 1-5-1 Chofugaoka, Chofu, Tokyo, 182-8585, Japan

H. Yoshida
Molecular Chirality Research Center, Chiba University, 1-33 Yayoi-cho, Inage-ku, Chiba, 263-8522, Japan

Contents

S1. Determining the energy levels of perovskite

S1.1. Ionization energy and electron affinity of perovskite

The ionization energy (IE) and the electron affinity (EA) of $Cs_{0.05}FA_{0.80}MA_{0.15}PbI_{2.75}Br_{0.25}$ (MixA-PVK1) and $MAPbI_3$ are determined from the UPS and LEIPS spectra (Figure S1). The intensity is plotted on a logarithmic scale[1,2]. The spectrum of $MAPbI_3$ is converted from a linear scale into a logarithmic one on the basis of the data reported in Ref. 3. The IE and EA of $FASnI_3$ were taken from Ref. 4. These values were also determined from the logarithmic scale UPS and LEIPS spectra.

It is noteworthy that IE can also be determined from photoemission yield spectroscopy (PYS). In fact, IE determined from PYS (5.56 eV for MixA-PVK1[5], 5.46 eV for $MAPbI_3$[6] and 5.16 eV for $FAPbI_3$[7]) shows close agreement with those obtained from the log-scale UPS. We propose the following explanation. Depending on the experimental setup (the detection angle of photoelectrons), the UPS sometimes cannot access the valence band (VB) edge due to the momentum conservation[2]. For example, the VB edge of $MAPbI_3$ is located at the R point, which cannot be directly measured by the normal emission UPS. Consequently very weak signals from the VB edge are resolved in the UPS spectrum plotted on the logarithmic scale[1,2]. Conversely, PYS detects photoelectrons emitted at all the angles by applying a high bias voltage to the electron detector. This enables the detection of the VB edge regardless of the momentum of the photoelectrons.

Unfortunately, UPS data on the logarithmic scale could not be obtained for $Cs_{0.05}FA_{0.73}MA_{0.22}PbI_{2.31}Br_{0.69}$ (MixA-PVK2). Therefore, the VB edge derived from the linear-scale spectra is used instead[8]. The conduction band (CB) edge of MixA-PVK2 is estimated from the onset of optical absorption.

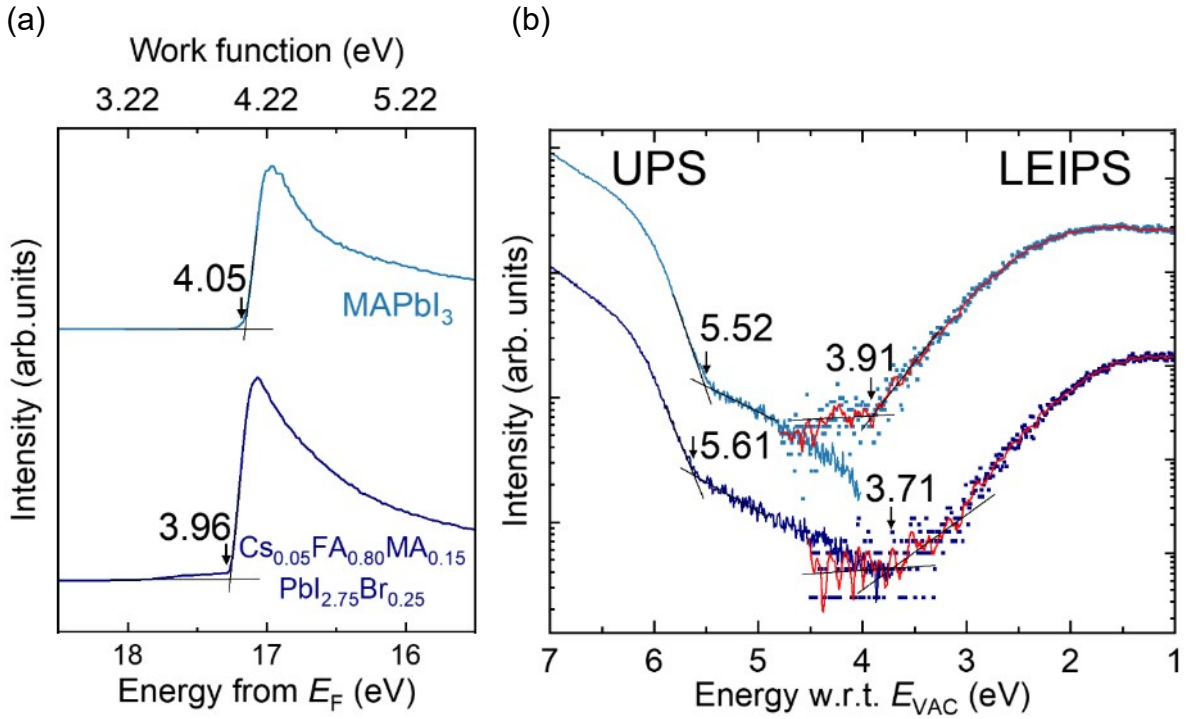

Figure S1. UPS and LEIPS spectra of $MAPbI_3$ and MixA-PVK1. (a) Secondary electron cut-off. (b) VB and CB regions.

S1.2. Work function of perovskite film deposited on different underlayers

The work function of perovskite can vary with that of the substrate[9–13]. Therefore, in this study, we examine whether the energy levels of perovskite films on ITO are suitable for evaluating the energy level alignment at the ITO/HCM/perovskite interfaces.

Figure S2a shows the UPS-measured work functions of MixA-PVK1 films deposited on ITO and HCM layers. The work functions are 3.96 eV on ITO, 3.89 eV on 2PACz, 3.93 eV on MeO-2PACz, and 3.96 eV on 3PATAT-C3. Figure S2b shows the correlation of the work function of perovskite on each HCM with that of HCM together with pyrene-based HCMs[14]. The perovskite work function remains nearly constant regardless of the substrate work function. We consider the following two factors to account for this observation.

- **The perovskite depletion region terminates within its layer thickness**

  Cahen et al. reported that the dopant density of high-quality perovskite solar cell devices rarely exceeds 10^{16} cm^{-3} [9]. Equation S1 gives the depletion width of a Schottky junction. ε_s is the (static) permittivity of the semiconductor (halide perovskite in this study), q is the electron charge, N_D is the dopant density, and V is the voltage difference across the sample. Assuming $\varepsilon_s \approx 30\ \varepsilon_o$ and $N_D = 10^{16}$ cm^{-3}, we obtain $W_D = 0.61$ μm for 2PACz, 0.47 μm for MeO-2PACz, and 0.51 μm for 3PATAT-C3. Here, the perovskite layer thickness is approximately 600–700 nm. Therefore, the work function measured by UPS represents the value at the termination of the depletion region. As a result, perovskite exhibits the same work function regardless of the underlying layer.

$$W = \sqrt{\frac{2\varepsilon_S V}{qN_D}} \qquad \text{(Equation S1)}$$

  In contrast, other studies reported that the perovskite work function varies with the substrate work function[10,11]. Those studies used thinner perovskite layers, typically 250–400 nm thick. The measured work function likely corresponds to an undeveloped depletion region. This explains its clear correlation with the substrate work function.

- **The intrinsic carrier density of this perovskite may be relatively high.**

  Zohar et al. reported that the work function of $Cs_{0.05}FA_{0.85}MA_{0.1}PbBr_3$ correlates with that of the substrate. In contrast, $MAPbBr_3$, $CsPbBr_3$, and $MAPbBr_{2.0}Cl_{1.0}$ show no such

correlation, owing to differences in their intrinsic carrier densities[10]. Because the perovskite used in this study likely has a relatively high intrinsic carrier density, its work function is not expected to correlate with that of the substrate.

In summary, we believe that the work function of the perovskite prepared on ITO can be adopted because the perovskite is sufficiently thick to be unaffected by the substrate work function or has a relatively high intrinsic carrier density. This work function value can therefore be applied to the present energy level alignment model.

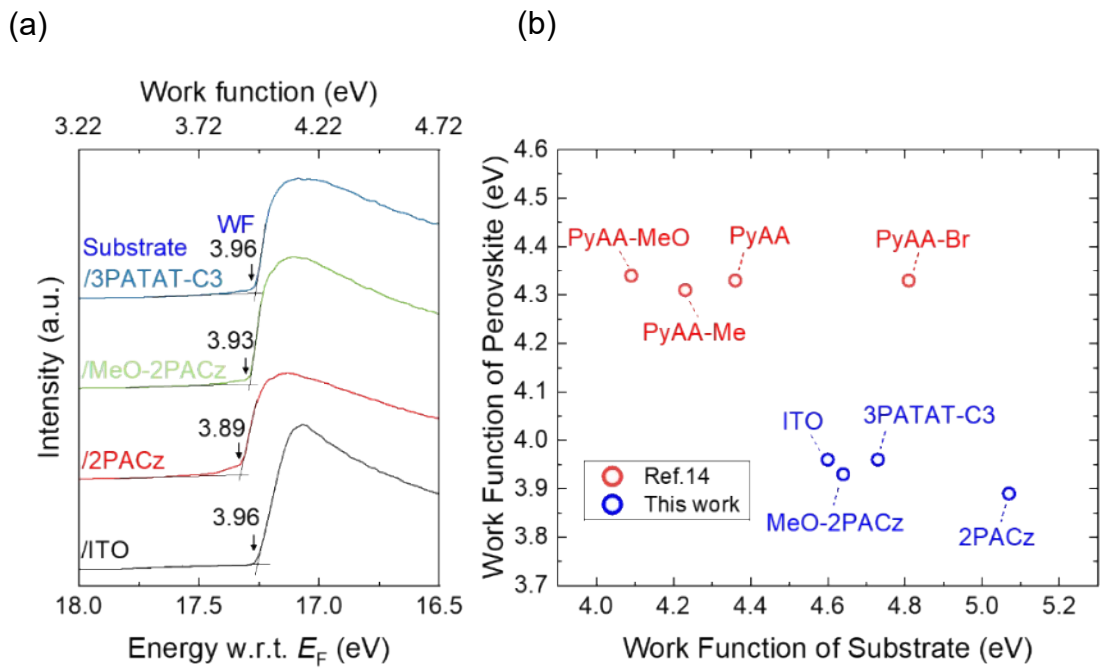

Figure S2. (a) Work functions of MixA-PVK1 films deposited on different underlayers, measured by UPS. (b) Plots of perovskite work function versus substrate work function.

S2. Details of previous models shown in Figure 1

S2.1. Vacuum alignment model

Figure S3 shows the energy levels of ITO, HCMs, and perovskites with reference to the vacuum level. For ITO, the difference between the Fermi level and the vacuum level is the work function, which is measured by UPS. For HCMs, the HOMO and LUMO levels with respect to the vacuum level are the IE and the EA, respectively, measured by UPS and LEIPS, as shown in Figure 2b. The VB and CB edges with respect to the vacuum level are the IE and the EA, as discussed in S1.1 of Supporting Information.

According to this model, the LUMO levels of all HCMs are located 1.81–2.72 eV above the CB edge of perovskites MixA-PVK2, $MAPbI_3$, and $FASnI_3$, indicating good electron-blocking capability. Regarding hole collection efficiency, the HOMO level of 3PATAT-C3 is nearly aligned with the VB edge of lead perovskites $MAPbI_3$ and MixA-PVK2. The HOMO level of MeO-2PACz lies 0.39 and 0.31 eV above the VB edge of these lead perovskites. In contrast, the HOMO level of 2PACz is located 0.24–0.32 eV below the VB edge. These results suggest good hole collection efficiency for MeO-2PACz and 3PATAT-C3 only. Regarding tin perovskite $FASnI_3$, the VB edge is located 0.23–0.53 eV above the HOMO levels of 2PACz and 3PATAT-C3 and 0.10 eV below the HOMO level of MeO-2PACz, yielding superior photovoltaic performance compared with 2PACz, as shown in Table S1.

This energy level diagram demonstrates the inferior photovoltaic performance of 2PACz (Figure 3 and Table 1). However, this model is too simplified, contradicting the observed vacuum level shift between the HCM and the electrode (Figure 2a), as discussed in the main text.

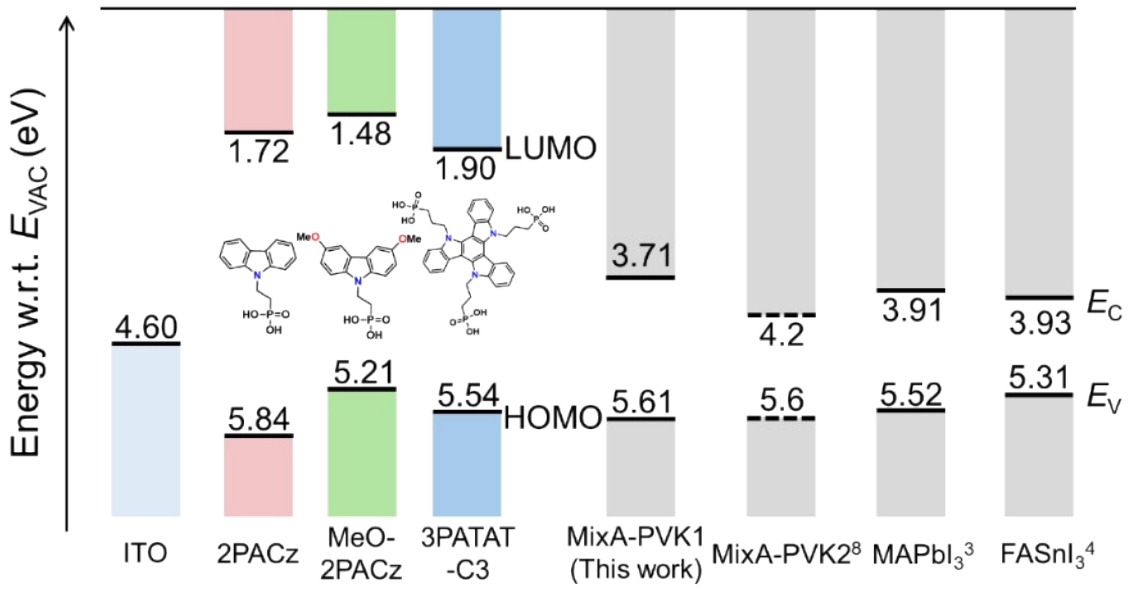

Figure S3. Energy level diagram of ITO, HCMs, and perovskites with reference to the vacuum level. MixA-PVK1 and MixA-PVK2 represent the perovskites with compositions $Cs_{0.05}FA_{0.80}MA_{0.15}PbI_{2.75}Br_{0.25}$ and $Cs_{0.05}FA_{0.73}MA_{0.22}PbI_{2.31}Br_{0.69}$, respectively. MixA-PVK 1 corresponds to the perovskite measured experimentally in this work. The solid and dashed lines of the VB edge of the perovskites are determined from the logarithmic and linear scales of UPS spectra, respectively. For the CB edge of the perovskites, the solid and dotted lines are determined from the logarithmic scales of LEIPS spectra and the optical band gap.

S2.2. Fermi level alignment model

The energy level diagram of this model is shown in Figure 2c. The LUMO levels of all HCMs are located at 1.93–3.21 eV above the CB edge of the perovskites. Except for the interface between the HCMs and $FASnI_3$, the HOMO levels of all HCMs are positioned 0.09–1.08 eV above the VB edge of the three lead perovskites. Although an interface dipole layer of 0.47 eV in 2PACz is observed, the HOMO and LUMO levels are similar among these HCMs. Therefore, this model cannot explain the difference in photovoltaic performance depending on the HCMs (Figure 3) and thus is not applicable to the HCM/perovskite interface.

S2.3. Schottky model considering the interface between HCM-modified electrode and perovskite

Figure S4 shows the energy level diagrams based on the Schottky model, in which HCM is treated as a work function modifier; that is, ITO/HCM is treated as an electrode. Figure S4a shows the energy level diagram for MixA-PVK1. A large upward band bending of 0.68–1.11 eV and a high hole collection efficiency are predicted. However, this model is not consistent with the poor photovoltaic performance of 2PACz. For MixA-PVK2 (Figure S4b), an upward band bending of 0.3 eV for 2PACz and 0.03 eV for 3PATAT-C3 is favorable for hole collection and electron blocking, whereas the small downward band bending of 0.1 eV for MeO-2PACz indicates poor electron blocking (The work function values of 2PACz and MeO-2PACz are taken from the literature. Ref. 8). Al-Ashouri et al. reported photovoltaic performance using 2PACz (PCE of 20.9%) and MeO-2PACz (20.4%)[8]. This difference in photovoltaic performance is, by chance, in good agreement with the Schottky model prediction because there is no energy barrier at the interface (Figure 5b).

As shown in Figure S4c, this model predicts an upward band bending of 0.59–1.02 eV for $MAPbI_3$, similar to that for the above-mentioned MixA-PVK1. Unfortunately, we cannot find literature comparing the photovoltaic performances of these HCMs with that of $MAPbI_3$. Finally, for $FASnI_3$, the band bending direction varies with HCM owing to the large work function of 4.83 eV (Figure S4d). For 2PACz, an upward band bending of 0.24 eV is predicted. In contrast, the downward band bending of 0.19 eV and 0.10 eV is expected for MeO-2PACz and 3PATAT-C3, respectively, indicating particularly low hole collection efficiency predicted for the latter. However, the device with MeO-2PACz exhibits a high PCE (Table S1), contradicting the Schottky model prediction.

(a)

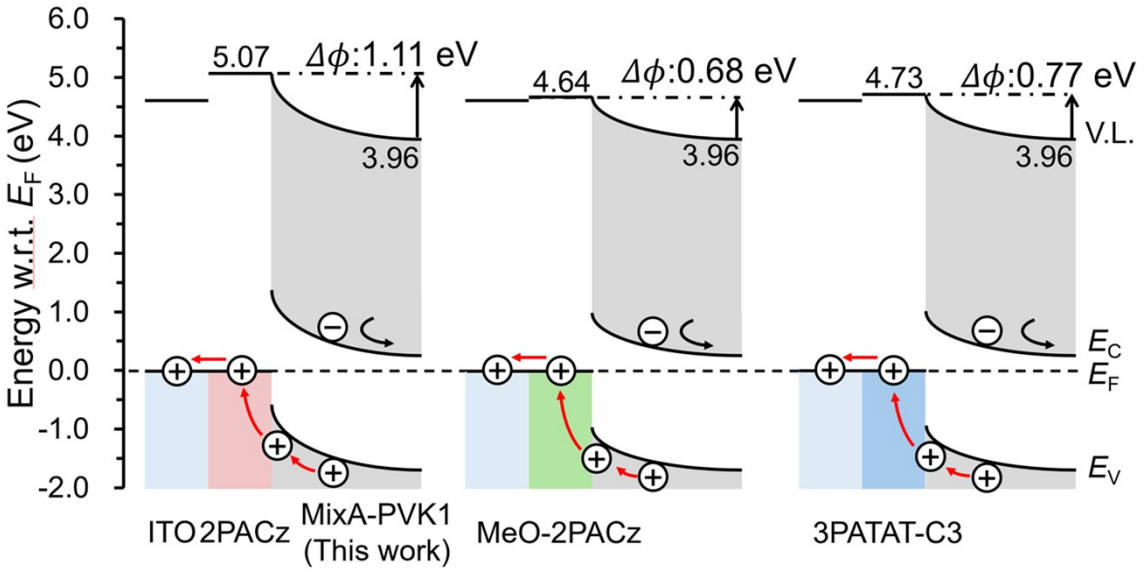
Energy w.r.t. E_F (eV)
6.0
5.0
4.0
3.0
2.0
1.0
0.0
-1.0
-2.0
5.07
$\Delta\phi$:1.11 eV
3.96
4.64
$\Delta\phi$:0.68 eV
3.96
4.73
$\Delta\phi$:0.77 eV
3.96
V.L.
E_C
E_F
E_V
ITO
2PACz
MixA-PVK1
(This work)
MeO-2PACz
3PATAT-C3

(b)

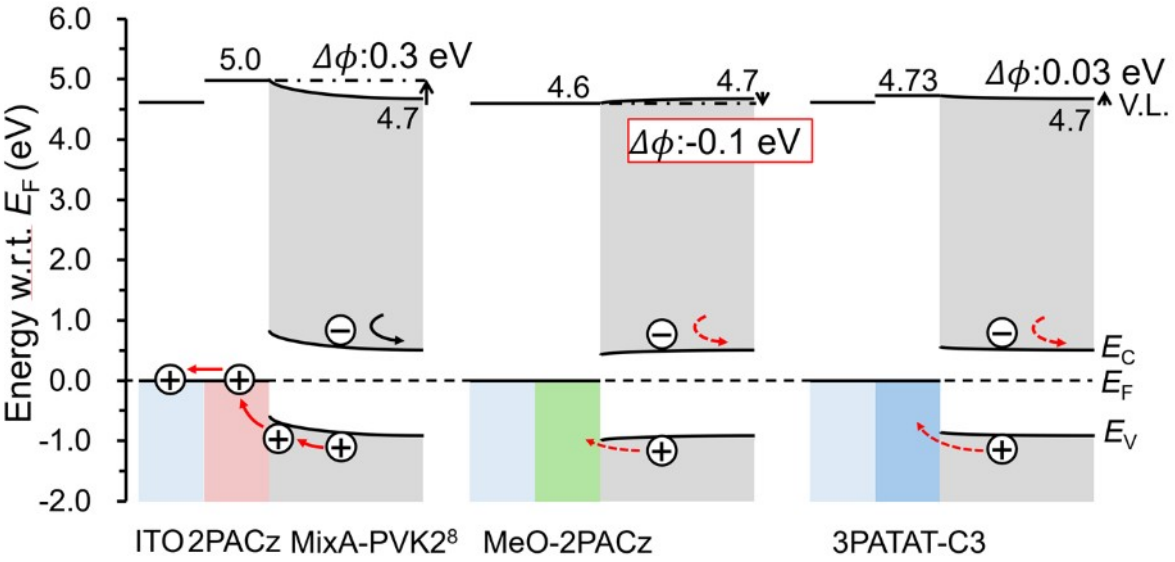
Energy w.r.t. E_F (eV)
6.0
5.0
4.0
3.0
2.0
1.0
0.0
-1.0
-2.0
5.0
$\Delta\phi$:0.3 eV
4.7
4.6
4.7
$\Delta\phi$:-0.1 eV
4.73
$\Delta\phi$:0.03 eV
4.7
V.L.
E_C
E_F
E_V
ITO
2PACz
MixA-PVK2[8]
MeO-2PACz
3PATAT-C3

(c)

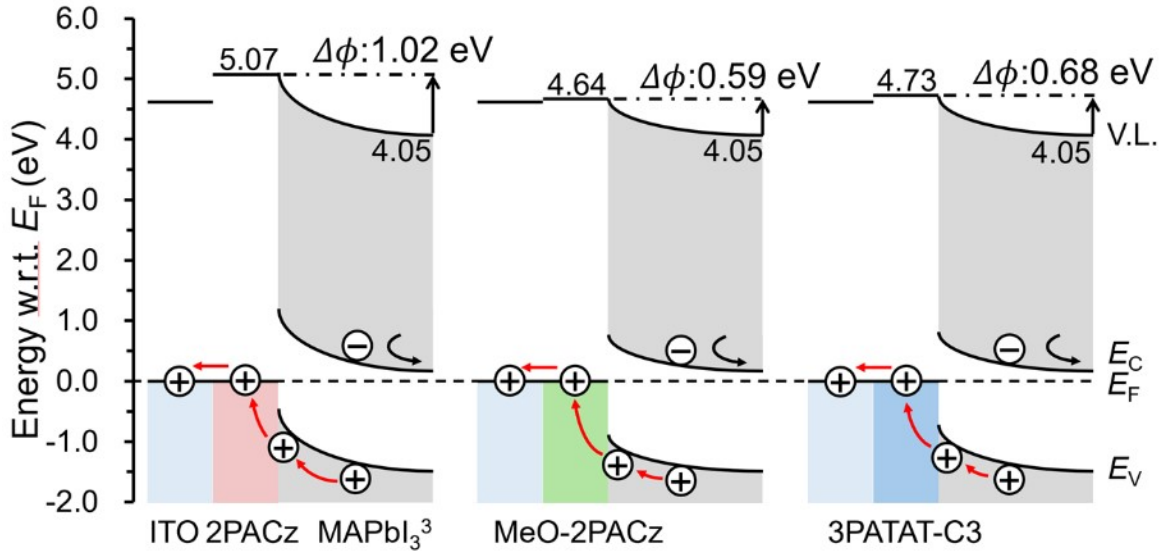

(d)

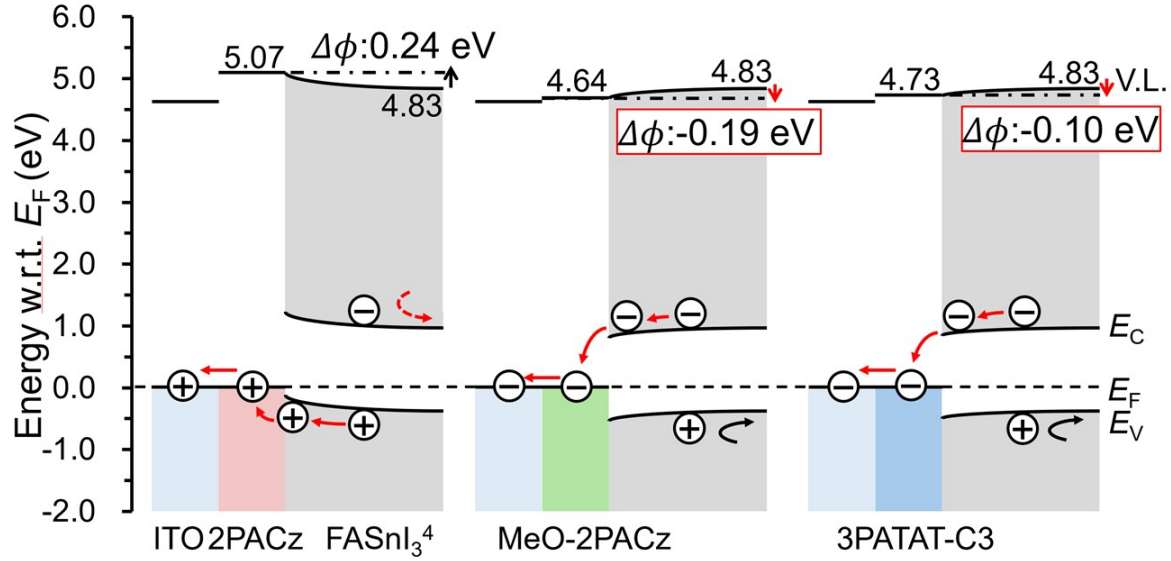

Figure S4. Schottky model for various perovskites. (a) MixA-PVK1, (b) MixA-PVK2, (c) $MAPbI_3$, and (d) $FASnI_3$

S3. Hole collecting layer/perovskite interface energy levels for $MAPbI_3$ and $FASnI_3$ based on the proposed model

Figures S5a and b show the interfacial energy level alignment for $MAPbI_3$ and $FASnI_3$, respectively, based on our proposed model, supplementing Figure 5 in the main text. Regarding the energy level diagram for PEDOT:PSS/$FASnI_3$, because the energy parameters of $FASnI_3$ have been reported along with the photovoltaic performance, we refer to Ref.15 to strengthen the reliability of our analysis. Table S1 summarizes band bending $\Delta\Phi$, barrier height ΔE_V, and photovoltaic performance when $FASnI_3$ is used as the perovskite layer. The relationship between solar cell performance and energy level alignment is discussed in Section 2.4 of the main text.

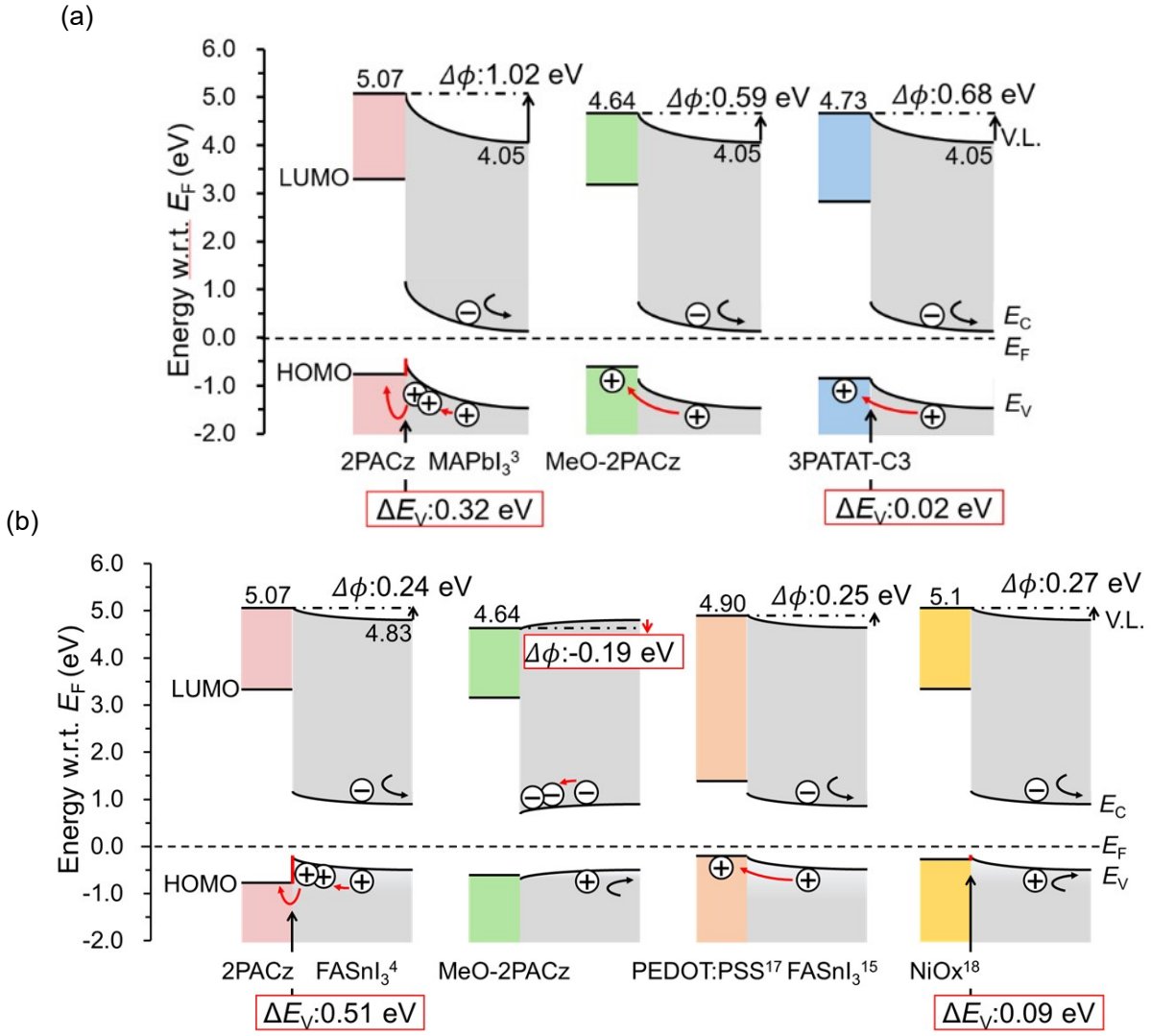

Figure S5. Energy level alignment of perovskite and HCMs based on our proposed model. (a) $MAPbI_3$ and (b) $FASnI_3$. For $FASnI_3$, typical hole collecting layers, PEDOT:PSS and NiO_x, are also shown in addition to HCMs.

Table S1. Performance parameters of $FASnI_3$ perovskite solar cells using different hole-collecting layers.

		Solar Cell Performance				Energy Parameters and Predicted efficiency		
HCM	Ref.	J_{SC} [mA/cm^2]	V_{OC} [V]	FF [%]	PCE [%]	Band bending[a] $\Delta\Phi$ [eV]	Barrier height[b] ΔE_V [eV]	Predicted hole collection efficiency[c]
2PACz	16	11.7	0.320	47.0	1.8	0.24	0.53	×
MeO-2PACz	16	16.7	0.403	60.8	4.1	-0.19	-0.10	×
PEDOT:PSS	15,17	21.19	0.66	0.67	9.38	**0.25**	**-0.07**	○
NiO_X	18,19	17.26	0.363	56.3	3.53	0.27	0.09	×

[a) and b)] A positive value means the upward band bending and the energy barrier for holes. [c)] ○ and × mean predicted high and low hole collection efficiencies, respectively.

S4. Validating the general applicability of the proposed energy level alignment model

S4.1. Comparison of UPS-derived valence band edge of perovskite using linear and logarithmic scales

Some studies reported only VB edge values derived from spectra plotted on a linear scale. Therefore, we compare VB edge values derived from spectra plotted on linear ($E_{V\text{-}Linear}$) and logarithmic ($E_{V\text{-}Log}$) scales to estimate $E_{V\text{-}Log}$ position systematically.

Figures S6a and b show the UPS spectra of MixA-PVK1 and $MAPbI_3$ plotted on both linear and logarithmic scales. The differences between $E_{V\text{-}Linear}$ and $E_{V\text{-}Log}$ are 0.25 eV and 0.28 eV, respectively, for the two perovskites. In addition, Zu et al. and Menzel et al. reported differences of 0.23 eV and 0.45 eV, respectively[2,20]. We assume that $E_{V\text{-}Log}$ is approximately 0.3 eV shallower than $E_{V\text{-}Linear}$ for literature data reporting only $E_{V\text{-}Linear}$, based on the average differences.

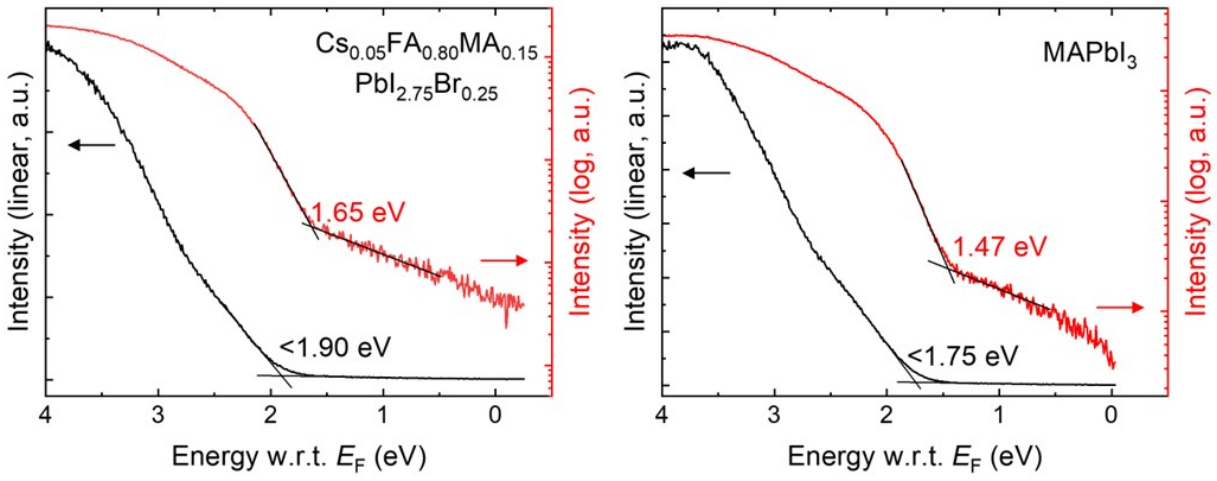

Figure S6. UPS spectra of perovskite are shown on both linear and logarithmic scales. (a) MixA-PVK1 and (b) $MAPbI_3$.

S4.2. Verification of universality of the proposed model

We test the universality of our model by comparing it with the reported photovoltaic performance of various HCM molecules, discussed in Section 2.5 of the main text. Here, we provide a detailed analysis of each set of HCMs using energy level diagrams constructed from our model. In the model, the energy barrier ΔE_{v} and the band bending $\Delta\Phi$ determine the hole collection efficiency. These quantities are derived from differences in ionization energy and work function, respectively, between HCM and perovskite. For the perovskite ionization energy, we use values determined from the VB edge on both linear $E_{\mathrm{v\text{-}Linear}}$ and logarithmic $E_{\mathrm{v\text{-}Log}}$ intensity scales. Except for the cases of 4PADCB[21] and 4-XPBA[22], only $E_{\mathrm{V\text{-}Linear}}$ values are reported. In these cases, $E_{\mathrm{v\text{-}Log}}$ is estimated using the method described in S4.1 of Supporting Information. Figures S7a–h show the energy level alignments at the HCM/perovskite interfaces. The evaluated hole collection efficiencies are compared with photovoltaic performance in Table 2 of the main text.

Figure S7a shows the energy level diagrams for Me-PhpPACz[23] and Me-4PACz. Neither HCM forms an energy barrier $\Delta E_{\mathrm{V\text{-}Linear}}$ at the HCM/perovskite interface when the barrier is derived from the linear-scale UPS spectrum. Conversely, for the log-scale spectrum, $\Delta E_{\mathrm{V\text{-}Log}}$ values are non-zero but small (below 0.1 eV). An upward band bending $\Delta\Phi$ of 0.53 eV is predicted for Me-PhpPACz, which is 0.10 eV larger than that for Me-4PACz. This indicates that Me-PhpPACz provides more favorable energy level alignment for efficient hole collection than Me-4PACz.

Figure S7b shows the energy level diagrams for Br-2EPT[24] and MeO-2PACz. No energy barrier $\Delta E_{\mathrm{V\text{-}Linear}}$ is expected for either molecule (a small negative $\Delta E_{\mathrm{V\text{-}Log}} < -0.1$ eV appears for Br-2EPT). However, forMeO-2P ACz, a large downward band bending $\Delta\Phi$ of 0.58 eV is predicted because of its low work function Φ_{HCM}. Consequently, lower photovoltaic performance is predicted for MeO-2PACz than for Br-2EPT.

Next, we examine MeO-BTBT[25] in comparison with MeO-2PACz (Figure S7c). On a linear scale, no energy barrier $\Delta E_{\mathrm{V\text{-}Linear}}$ is expected for either molecule, whereas a moderate barrier $\Delta E_{\mathrm{V\text{-}Log}}$ of 0.14 eV is formed only in MeO-BTBT. This may be because the perovskite energy levels were not measured in the same study[26]. It is preferable that the energy parameters of HCM and perovskite be measured simultaneously. MeO-BTBT exhibits an upward band bending $\Delta\Phi$ of 0.21 eV, which is 0.11 eV larger than that of MeO-2PACz. This suggests that MeO-BTBT provides more favorable energy level alignment for hole collection than MeO-2PACz.

The energy level diagrams for 4PADCB and 4PACz[21] are shown in Figure S7d. Both HCMs show small downward band bending $\Delta\Phi$. However, 4PACz exhibits a large energy barrier $\Delta E_{V\text{-}Log}$ of 0.27 eV, whereas 4PADCB shows no $\Delta E_{V\text{-}Log}$ barrier. This indicates that hole collection is higher in 4PADCB than in 4PACz.

The energy level diagram for IDCz[27] is shown in Figure S7e. There are no energy barriers ($\Delta E_{V\text{-}Linear}$ or $E_{V\text{-}Log}$) for any of these molecules, indicating that the hole collection efficiencies are governed by band bending. $\Delta\Phi$ is downward for IDCz-1 and upward for IDCz-2 and IDCz-3, the latter showing the largest upward $\Delta\Phi$ of 0.27 eV. The predicted order of hole collection efficiencies is IDCz-1 < IDCz-2 < IDCz-3, in good agreement with the observed photovoltaic performance (Table 2 of the main text).

The energy level diagram for Py3[28] is compared with that for 2PACz in Figure S7f. No energy barrier $\Delta E_{V\text{-}Linear}$ is formed for either molecule. Given the magnitude of $\Delta\Phi$, 2PACz is expected to exhibit superior solar cell performance; however, this result contradicts the actual photovoltaic performance, likely due to the method used to determine VB edge. When the $E_{V\text{-}Log}$ is used for this test, a large energy barrier $\Delta E_{V\text{-}Log}$ of 0.23 eV is predicted only for 2PACz. Given that band bending is downward in both cases, the barrier ΔE_V observed only for 2PACz can account for the relative difference in photovoltaic performance between the two molecules.

Next, Figure S7g shows the energy level diagrams for a series of donor–acceptor-type HCMs, MPA-BT-XA (X = C, B, and R)[29]. Although the energy parameters of the perovskite layer were obtained from publication by the same group[30], no energy barriers $\Delta E_{V\text{-}Linear}$ were predicted for any of them. If the log-scale value $E_{V\text{-}Log}$ is applied, negligible barriers $\Delta E_{V\text{-}Log}$ of up to 0.1 eV appear for all. MPA-BT-CA exhibits the largest upward band bending $\Delta\Phi$ of 0.73 eV, followed by MPA-BT-BA and MPA-BT-RA. The photovoltaic performance follows the same order, MPA-BT-RA < MPA-BT-BA < MPA-BT-CA.

Finally, Figure S7h shows the energy level diagrams for 4-XPBA (X = N, C, TF, and F)[22], with MeO-2PACz used as the reference. In this work, FTO is used as the electrode. At the pristine FTO/perovskite interface, downward band bending $\Delta\Phi$ is predicted, hindering efficient hole collection. In contrast, upward $\Delta\Phi$ is calculated with magnitudes of the order MeO-2PACz ($\Delta\Phi$ = 0.38 eV) > 4-NPBA (0.33 eV) > 4-CPBA (0.28 eV) > 4-TFPBA (0.12 eV) > 4-FPBA (0.08 eV). Meanwhile, barriers $\Delta E_{V\text{-}Log}$ are quite large for 4-XPBA (1.3–1.5 eV) and moderate for MeO-2PACz (0.18 eV). From these results, one can predict the best photovoltaic performance for MeO-2PACz; however, the actual photovoltaic performance does not follow

this trend (Table 2 of the main text). We interpret this discrepancy by considering the low surface coverage of the 4-XPBA series. Based on XPS signal intensities, we estimate that the surface-adsorbed density of 4-XPBA is approximately one-quarter of that of MeO-2PACz. Consequently, holes are collected through the HOMO of MeO-2PACz owing to its dense layer. In contrast, in the sparsely covered 4-XPBA films, holes are collected through the uncovered electrode regions. This indicates that 4-XPBA acts not as a semiconductor but as a work function modifier (see Ref. 22 for details).

Based on the above discussions, our proposed model is broadly applicable not only to carbazole derivatives but also to other HCMs. Furthermore, with minor corrections, the model can be applied to systems with low surface coverage, supporting its universality. We confirm that relative comparisons within the same study remain valid.

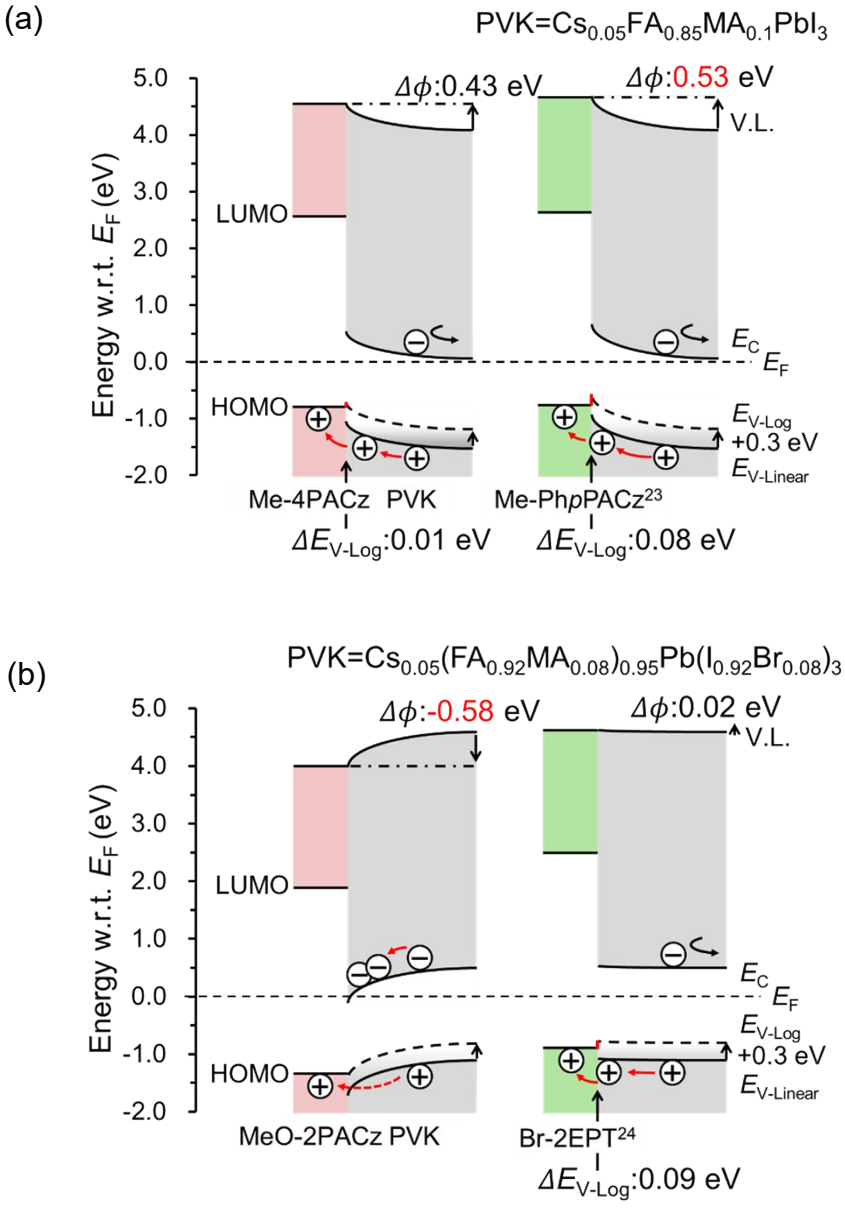

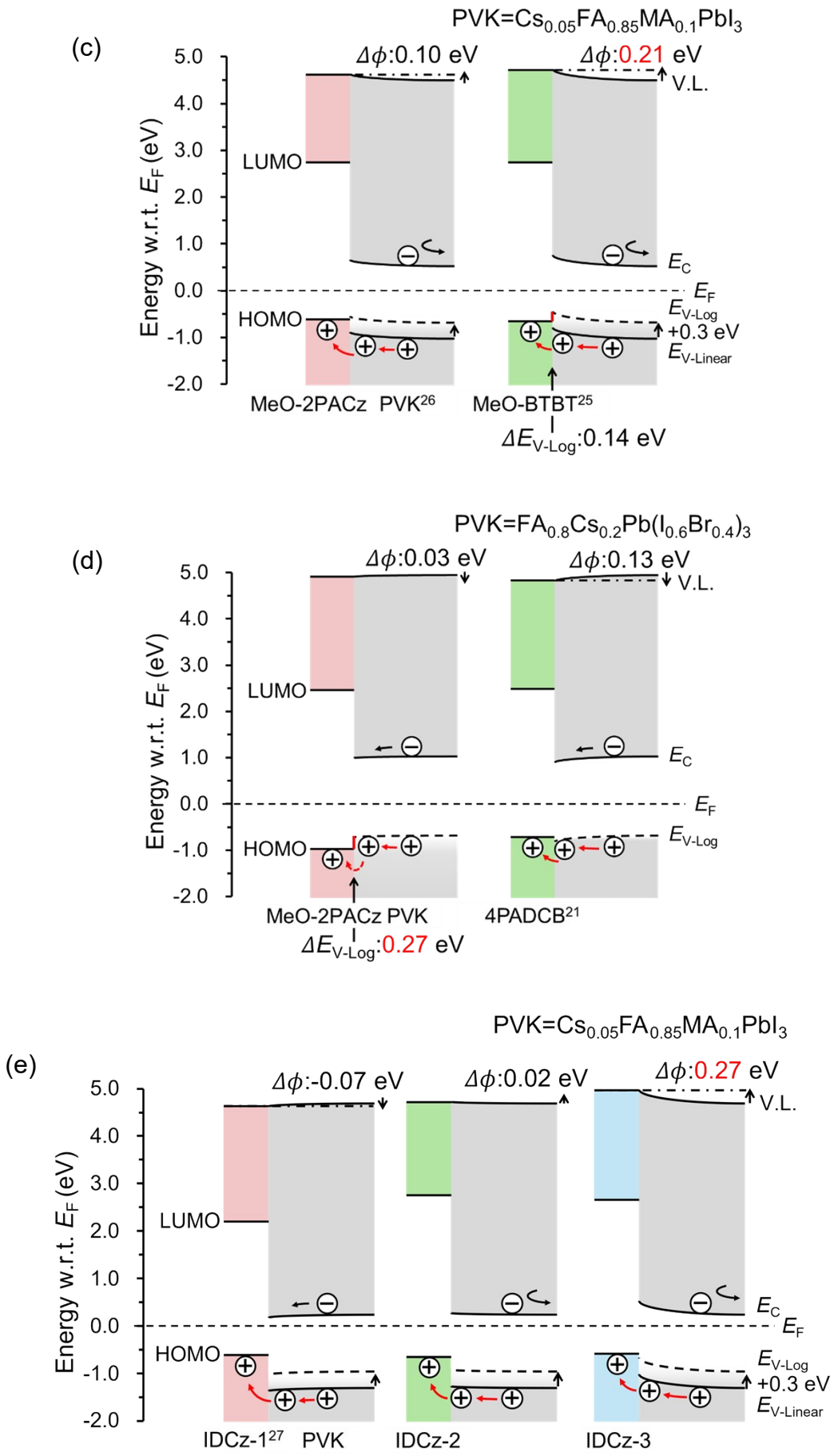
(c)
PVK=Cs0.05FA0.85MA0.1PbI3
Δϕ:0.10 eV
Δϕ:0.21 eV
V.L.
LUMO
EC
EF
EV-Log
+0.3 eV
EV-Linear
HOMO
MeO-2PACz
PVK26
MeO-BTBT25
ΔEV-Log:0.14 eV
Energy w.r.t. EF (eV)
5.0
4.0
3.0
2.0
1.0
0.0
-1.0
-2.0
(d)
PVK=FA0.8Cs0.2Pb(I0.6Br0.4)3
Δϕ:0.03 eV
Δϕ:0.13 eV
V.L.
LUMO
EC
EF
EV-Log
HOMO
MeO-2PACz
PVK
4PADCB21
ΔEV-Log:0.27 eV
Energy w.r.t. EF (eV)
5.0
4.0
3.0
2.0
1.0
0.0
-1.0
-2.0
(e)
PVK=Cs0.05FA0.85MA0.1PbI3
Δϕ:-0.07 eV
Δϕ:0.02 eV
Δϕ:0.27 eV
V.L.
LUMO
EC
EF
EV-Log
+0.3 eV
EV-Linear
HOMO
IDCz-127
PVK
IDCz-2
IDCz-3
Energy w.r.t. EF (eV)
5.0
4.0
3.0
2.0
1.0
0.0
-1.0
-2.0

(f)

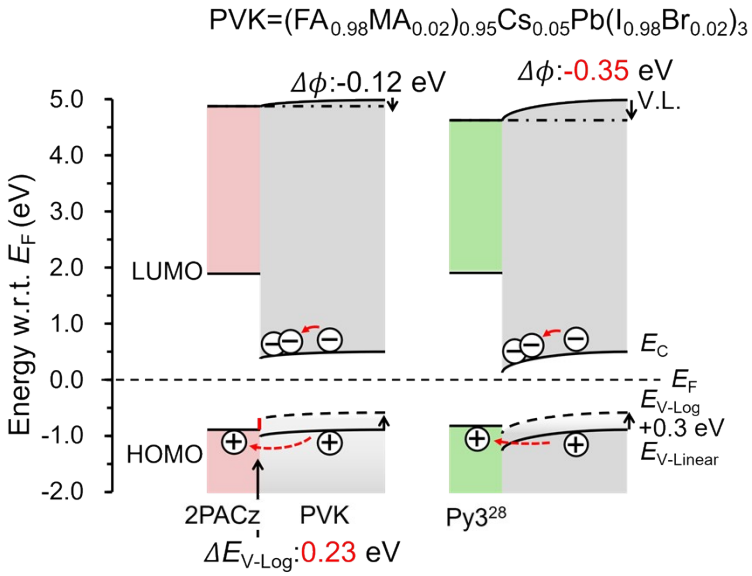
PVK=(FA0.98MA0.02)0.95Cs0.05Pb(I0.98Br0.02)3
Δϕ:-0.12 eV
Δϕ:-0.35 eV
V.L.
Energy w.r.t. EF (eV)
5.0
4.0
3.0
2.0
1.0
0.0
-1.0
-2.0
LUMO
HOMO
EC
EF
EV-Log
+0.3 eV
EV-Linear
2PACz
PVK
Py3[28]
ΔEV-Log:0.23 eV

(g)

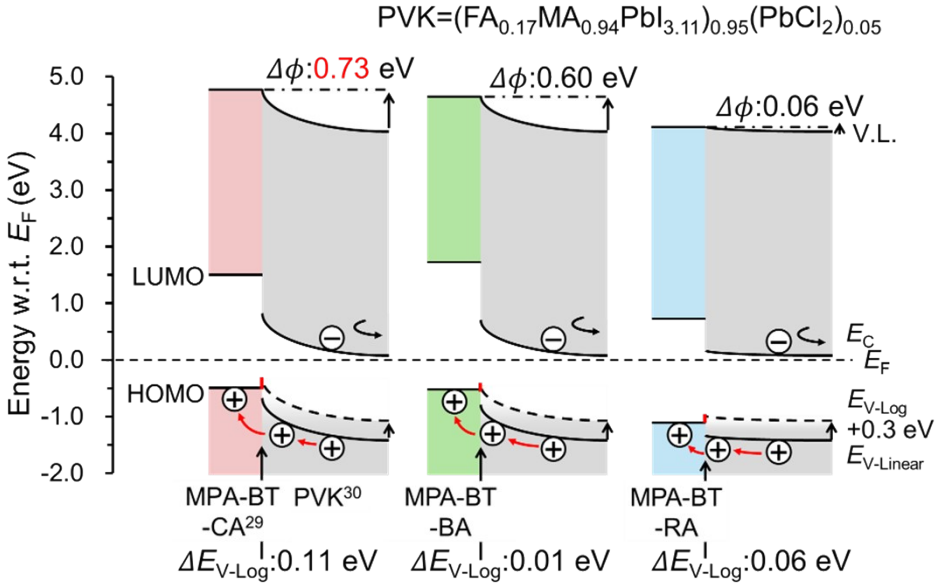
PVK=(FA0.17MA0.94PbI3.11)0.95(PbCl2)0.05
Δϕ:0.73 eV
Δϕ:0.60 eV
Δϕ:0.06 eV
V.L.
Energy w.r.t. EF (eV)
5.0
4.0
3.0
2.0
1.0
0.0
-1.0
-2.0
LUMO
HOMO
EC
EF
EV-Log
+0.3 eV
EV-Linear
MPA-BT -CA[29]
PVK[30]
MPA-BT -BA
MPA-BT -RA
ΔEV-Log:0.11 eV
ΔEV-Log:0.01 eV
ΔEV-Log:0.06 eV

(h)

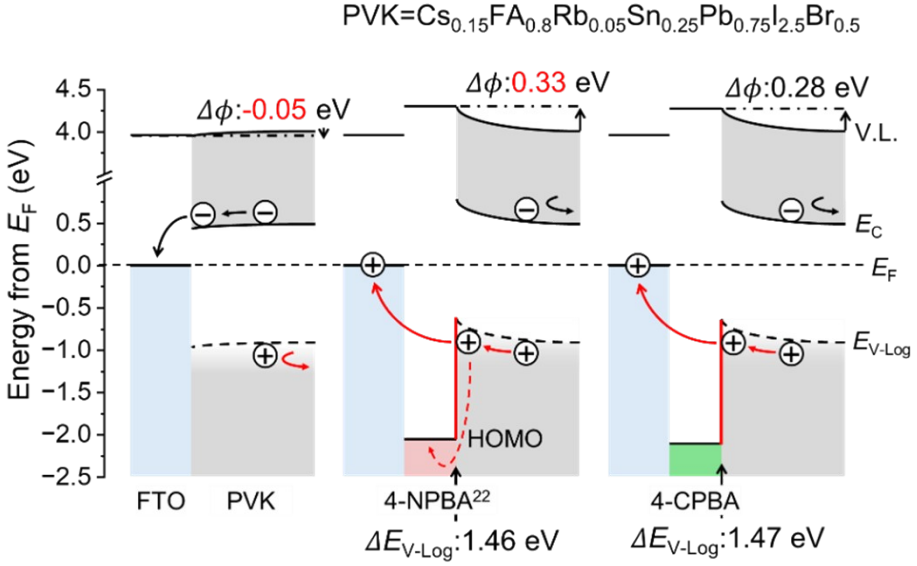
PVK=Cs0.15FA0.8Rb0.05Sn0.25Pb0.75I2.5Br0.5
Δϕ:-0.05 eV
Δϕ:0.33 eV
Δϕ:0.28 eV
V.L.
Energy from EF (eV)
4.5
4.0
0.5
0.0
−0.5
−1.0
−1.5
−2.0
−2.5
EC
EF
EV-Log
HOMO
FTO
PVK
4-NPBA[22]
4-CPBA
ΔEV-Log:1.46 eV
ΔEV-Log:1.47 eV

(h)

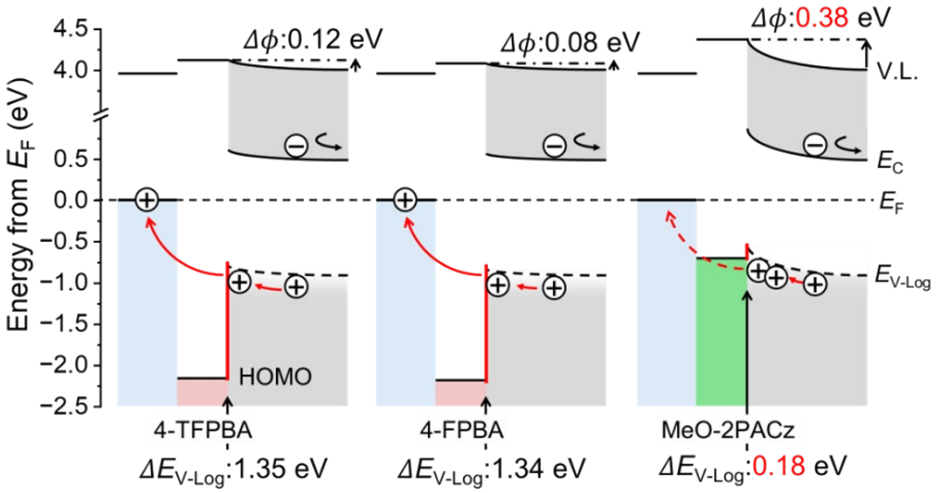

Figure S7. Energy-level alignment at the HCM/perovskite interface based on our proposed model. (a) Me-4PACz and Me-PhpPACz, (b) MeO-2PACz and Br-2EPT, (c) MeO-2PACz and MeO-BTBT, (d) 4PACz and 4PADCB, (e) IDCz-1, IDCz-2 and IDCz-3, (f) 2PACz and Py3, (g) MPA-BT-CA, MPA-BT-BA and MPA-BT-RA, and (h) FTO, 4NPBA, 4CPBA, 4TFPBA, 4FPBA and MeO-2PACz.

S5. Principles of molecular orientation analysis using UPS and MAES

Figure S8 shows the schematic of UPS and MAES spectra for different molecular orientations. As UPS utilizes ultraviolet photons as the excitation source, the probing depth is limited to a few nanometers by the elastic mean free path of electrons. Conversely, MAES utilizes metastable atoms (He*) instead of ultraviolet photons as the excitation source. These atoms only interact with the outermost orbitals of the samples, realizing extremely surface-sensitive measurement.

For planar π-conjugated molecules, both σ and π orbitals of the HCM molecules are observed in UPS, regardless of the molecular orientation. In contrast, the signal intensity is dependent on the orbital nature in MAES. When molecules adopt a parallel orientation to the substrate surface, the metastable atoms strongly interact with the π orbitals, resulting in a prominent π peak (upper panel). When molecules adopt a perpendicular orientation, He* interacts with the σ orbitals, leading to a noticeable σ peak (lower panel). Therefore, we can determine the molecular orientation by comparing the intensity of the π or σ orbital peaks in the MAES spectrum with that in the UPS spectrum.

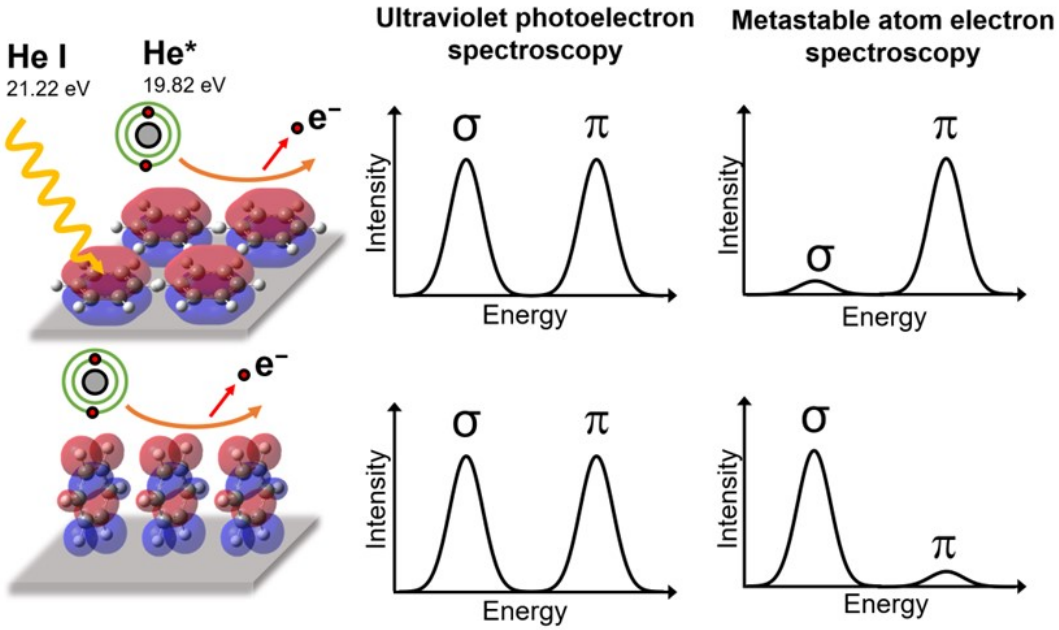

Figure S8. Schematic of UPS and MAES spectra for different molecular orientations. Upper and lower illustrations represent the shapes of the UPS and MAES spectra when HCM molecules adopt a parallel orientation and a perpendicular orientation to the substrate surface, respectively.

Figure S9 shows examples of molecular orbital classification for reproducing the spectrum corresponding to each orbital. The orbitals are calculated using the density functional theory (DFT) method with the B3LYP functional and the 6-31G(d) basis set on the Gaussian 16 program.

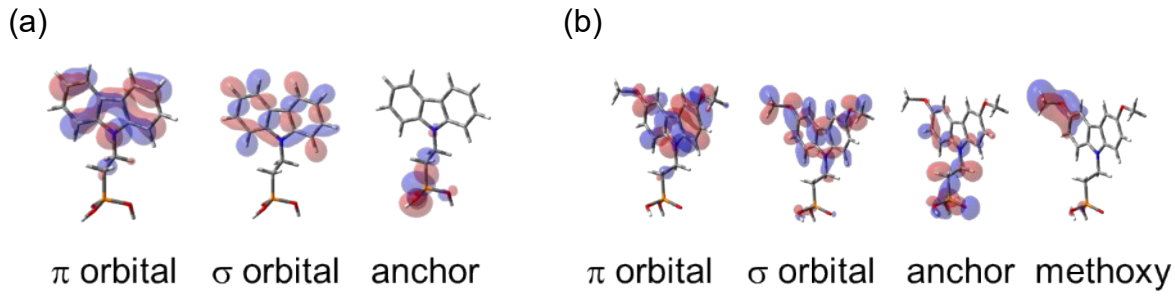

Figure S9. Examples of molecular orbital classification for (a) 2PACz and (b) MeO-2PACz.

S6. Calculation of electrostatic energy and polarization energy

The electrostatic energy and the polarization energy are calculated using the following equations (Equation S2), respectively[31],

$$S = \frac{I_g + A_g - (I_S + A_S) - \Delta_+ + \Delta_-}{2}$$
$$D = \frac{I_g - A_g - (I_S - A_S) - \Delta_+ - \Delta_-}{2} \quad \text{(Equation S2)}$$

where I and A are the ionization energy and the electron affinity, respectively. Subscripts 'g' and 's' represent the gas phase and solid phase, respectively. Δ_+ and Δ_- are corrections from the HOMO and LUMO bandwidths, respectively, owing to the intermolecular quantum mechanical electronic coupling. The terms Δ_+ and Δ_- were ignored in this work.

References

1 J. Endres, D. A. Egger, M. Kulbak, R. A. Kerner, L. Zhao, S. H. Silver, G. Hodes, B. P. Rand, D. Cahen, L. Kronik and A. Kahn, Valence and conduction band densities of states of metal halide perovskites: A combined experimental–theoretical study, *J. Phys. Chem. Lett.*, 2016, **7**, 2722–2729.

2 F. Zu, P. Amsalem, D. A. Egger, R. Wang, C. M. Wolff, H. Fang, M. A. Loi, D. Neher, L. Kronik, S. Duhm and N. Koch, Constructing the electronic structure of $CH_3NH_3PbI_3$ and $CH_3NH_3PbBr_3$ perovskite thin films from single-crystal band structure measurements, *J. Phys. Chem. Lett.*, 2019, **10**, 601–609.

3 A. Mirzehmet, T. Ohtsuka, S. A. Abd. Rahman, T. Yuyama, P. Krüger and H. Yoshida, Surface termination of solution-processed $CH_3NH_3PbI_3$ perovskite film examined using electron spectroscopies, *Adv. Mater.*, 2021, **33**, 2004981.

4 A. M. Boehm, T. Liu, S. M. Park, A. Abtahi and K. R. Graham, Influence of surface ligands on energetics at $FASnI_3/C_{60}$ interfaces and their impact on photovoltaic performance, *ACS Appl. Mater. Interfaces*, 2020, **12**, 5209–5218.

5 M. Ozaki, Y. Ishikura, M. A. Truong, J. Liu, I. Okada, T. Tanabe, S. Sekimoto, T. Ohtsuki, Y. Murata, R. Murdey and A. Wakamiya, Iodine-rich mixed composition perovskites optimised for tin(IV) oxide transport layers: the influence of halide ion ratio, annealing time, and ambient air aging on solar cell performance, *J. Mater. Chem. A*, 2019, **7**, 16947–16953.

6 S. Ryu, J. H. Noh, N. J. Jeon, Y. Chan Kim, W. S. Yang, J. Seo and S. I. Seok, Voltage output of efficient perovskite solar cells with high open-circuit voltage and fill factor, *Energy Environ. Sci.*, 2014, **7**, 2614–2618.

7 M. Ozaki, Y. Katsuki, J. Liu, T. Handa, R. Nishikubo, S. Yakumaru, Y. Hashikawa, Y. Murata, T. Saito, Y. Shimakawa, Y. Kanemitsu, A. Saeki and A. Wakamiya, Solvent-coordinated tin halide complexes as purified precursors for tin-based perovskites, *ACS Omega*, 2017, **2**, 7016–7021.

8 A. Al-Ashouri, A. Magomedov, M. Roß, M. Jošt, M. Talaikis, G. Chistiakova, T. Bertram, J. A. Márquez, E. Köhnen, E. Kasparavičius, S. Levcenco, L. Gil-Escrig, C. J. Hages, R. Schlatmann, B. Rech, T. Malinauskas, T. Unold, C. A. Kaufmann, L. Korte, G. Niaura, V. Getautis and S. Albrecht, Conformal monolayer contacts with lossless interfaces for perovskite single junction and monolithic tandem solar cells, *Energy Environ. Sci.*, 2019, **12**, 3356–3369.

9 D. Cahen, Y. Rakita, D. A. Egger and A. Kahn, Surface defects control bulk carrier densities in polycrystalline Pb-halide perovskites, *Adv. Mater.*, 2024, **36**, 2407098.

10 A. Zohar, M. Kulbak, I. Levine, G. Hodes, A. Kahn and D. Cahen, What limits the open-circuit voltage of bromide perovskite-based solar cells?, *ACS Energy Lett.*, 2019, **4**, 1–7.

11 S. Olthof, Research update: The electronic structure of hybrid perovskite layers and their energetic alignment in devices, *APL Mater.*, 2016, **4**, 091502.

12 P. Schulz, L. L. Whittaker-Brooks, B. A. MacLeod, D. C. Olson, Y.-L. Loo and A. Kahn, Electronic level alignment in inverted organometal perovskite solar cells, *Adv. Mater. Interfaces*, 2015, **2**, 1400532.

13 E. M. Miller, Y. Zhao, C. C. Mercado, S. K. Saha, J. M. Luther, K. Zhu, V. Stevanović, C. L. Perkins and J. van de Lagemaat, Substrate-controlled band positions in $CH_3NH_3PbI_3$ perovskite films, *Phys. Chem. Chem. Phys.*, 2014, **16**, 22122–22130.

14 Y. Luo, Y. Tian, K. Zhao, W. Mao, C. Liu, J. Shen, Z. Cheng, C. Değer, X. Miao, Z. Zhang, X. Sun, L. Yao, X. Zhang, P. Shi, D. Jin, J. Deng, M. Tian, I. Yavuz, N. Dong, R. Liu, R. Wang, D. Yang and J. Xue, Inductive effects in molecular contacts enable wide-bandgap perovskite cells for efficient perovskite/TOPCon tandems, *Nat. Commun.*, 2025, **16**, 4516.

15 B.-B. Yu, Z. Chen, Y. Zhu, Y. Wang, B. Han, G. Chen, X. Zhang, Z. Du and Z. He, Heterogeneous 2D/3D tin-halides perovskite solar cells with certified conversion efficiency breaking 14%, *Adv. Mater.*, 2021, **33**, 2102055.

16 D. Song, S. Narra, M.-Y. Li, J.-S. Lin and E. W.-G. Diau, Interfacial engineering with a hole-selective self-assembled monolayer for tin perovskite solar cells via a two-step fabrication, *ACS Energy Lett.*, 2021, **6**, 4179–4186.

17 J. C. Yu, J. A. Hong, E. D. Jung, D. B. Kim, S.-M. Baek, S. Lee, S. Cho, S. S. Park, K. J. Choi and M. H. Song, Highly efficient and stable inverted perovskite solar cell employing PEDOT:GO composite layer as a hole transport layer, *Sci. Rep.*, 2018, **8**, 1070.

18 H. Zhang, J. Cheng, F. Lin, H. He, J. Mao, K. S. Wong, A. K.-Y. Jen and W. C. H. Choy, Pinhole-free and surface-nanostructured NiOx film by room-temperature solution process for high-performance flexible perovskite solar cells with good stability and reproducibility, *ACS Nano*, 2016, **10**, 1503–1511.

19 Q. Tai, X. Guo, G. Tang, P. You, T.-W. Ng, D. Shen, J. Cao, C.-K. Liu, N. Wang, Y. Zhu, C.-S. Lee and F. Yan, Antioxidant grain passivation for air-stable tin-based perovskite solar cells, *Angew. Chem. Int. Ed.*, 2019, **58**, 806–810.

20 D. Menzel, A. Tejada, A. Al-Ashouri, I. Levine, J. A. Guerra, B. Rech, S. Albrecht and L. Korte, Revisiting the determination of the valence band maximum and defect formation in halide perovskites for solar cells: Insights from highly sensitive near–UV photoemission spectroscopy, *ACS Appl. Mater. Interfaces*, 2021, **13**, 43540–43553.

21 R. He, W. Wang, Z. Yi, F. Lang, C. Chen, J. Luo, J. Zhu, J. Thiesbrummel, S. Shah, K. Wei, Y. Luo, C. Wang, H. Lai, H. Huang, J. Zhou, B. Zou, X. Yin, S. Ren, X. Hao, L. Wu, J. Zhang, J. Zhang, M. Stolterfoht, F. Fu, W. Tang and D. Zhao, Improving interface quality for 1-cm² all-perovskite tandem solar cells, *Nature*, 2023, **618**, 80–86.

22 S. Pradhan, H. Bì, G. Kapil, A. Akatsuka, A. K. Baranwal, D. Wang, D. Liu, S. Shaban, T. Kitamura, S. R. Sahamir, Y. Fujiwara, J. Liu, H. Segawa, H. Yoshida, Q. Shen and S. Hayase, Interfacial dipole engineering via boronic acid-based self-assembled monolayers in inverted tin–lead perovskite solar cells with ideal band gap, *ACS Energy Lett.*, 2025, **10**, 4983–4994.

23 G. Qu, S. Cai, Y. Qiao, D. Wang, S. Gong, D. Khan, Y. Wang, K. Jiang, Q. Chen, L. Zhang,

Y.-G. Wang, X. Chen, A. K.-Y. Jen and Z.-X. Xu, Conjugated linker-boosted self-assembled monolayer molecule for inverted perovskite solar cells, *Joule*, 2024, **8**, 2123–2134.

24 A. Ullah, K. H. Park, H. D. Nguyen, Y. Siddique, S. F. A. Shah, H. Tran, S. Park, S. I. Lee, K.-K. Lee, C.-H. Han, K. Kim, S. Ahn, I. Jeong, Y. S. Park and S. Hong, Novel phenothiazine-based self-assembled monolayer as a hole selective contact for highly efficient and stable p-i-n perovskite solar cells, *Adv. Energy Mater.*, 2022, **12**, 2103175.

25 M. Liu, M. Li, Y. Li, Y. An, Z. Yao, B. Fan, F. Qi, K. Liu, H.-L. Yip, F. R. Lin and A. K.-Y. Jen, Defect-passivating and stable benzothiophene-based self-assembled monolayer for high-performance inverted perovskite solar cells, *Adv. Energy Mater.*, 2024, **14**, 2303742.

26 J. Zeng, Z. Liu, D. Wang, J. Wu, P. Zhu, Y. Bao, X. Guo, G. Qu, B. Hu, X. Wang, Y. Zhang, L. Yan, A. K.-Y. Jen and B. Xu, Small-molecule hole transport materials for >26% efficient inverted perovskite solar cells, *J. Am. Chem. Soc.*, 2025, **147**, 725–733.

27 J. Wu, P. Yan, D. Yang, H. Guan, S. Yang, X. Cao, X. Liao, P. Ding, H. Sun and Z. Ge, Bisphosphonate-anchored self-assembled molecules with larger dipole moments for efficient inverted perovskite solar cells with excellent stability, *Adv. Mater.*, 2024, **36**, 2401537.

28 K. Zhao, Q. Liu, L. Yao, C. Değer, J. Shen, X. Zhang, P. Shi, Y. Tian, Y. Luo, J. Xu, J. Zhou, D. Jin, S. Wang, W. Fan, S. Zhang, S. Chu, X. Wang, L. Tian, R. Liu, L. Zhang, I. Yavuz, H. Wang, D. Yang, R. Wang and J. Xue, *peri*-Fused polyaromatic molecular contacts for perovskite solar cells, *Nature*, 2024, **632**, 301–306.

29 Q. Liao, Y. Wang, Z. Zhang, K. Yang, Y. Shi, K. Feng, B. Li, J. Huang, P. Gao and X. Guo, Self-assembled donor–acceptor hole contacts for inverted perovskite solar cells with an efficiency approaching 22%: The impact of anchoring groups, *J. Energy Chem.*, 2022, **68**, 87–95.

30 Q. Liao, Y. Wang, X. Yao, M. Su, B. Li, H. Sun, J. Huang and X. Guo, A dual-functional conjugated polymer as an efficient hole-transporting layer for high-performance inverted perovskite solar cells, *ACS Appl. Mater. Interfaces*, 2021, **13**, 16744–16753.

31 K. Yamada, S. Yanagisawa, T. Koganezawa, K. Mase, N. Sato and H. Yoshida, Impact of the molecular quadrupole moment on ionization energy and electron affinity of organic thin films: Experimental determination of electrostatic potential and electronic polarization energies, *Phys. Rev. B*, 2018, **97**, 245206.